The effect of nitrogen annealing on lithium ion intercalation in nickel-doped lithium trivanadate

Yaguang Liu · Cuiping Zhang · Chaofeng Liu ·
Huanqiao Song · Xihui Nan · Guozhong Cao

Abstract The communication reports an exploratory experimental study on the effects of nitrogen annealing on lithium ion intercalation in nickel-doped lithium trivanadate cathodic electrodes for lithium ion batteries. It shows good rate performance with discharge capacities of 348.6, 252.6, 191.9 and 96.7 mAh g^{-1} at 0.2, 0.5, 1 and 5 C, respectively. Nitrogen annealing resulted in the formation of parasitic secondary-phase LiV_2O_5 and appreciably increased tetravalent vanadium ions compensated with oxygen vacancies, which would enhance the electronic conductivity and lithium ion diffusivity and promote the interface interaction and deintercalation process, and thus lead to the enhanced lithium ion intercalation properties. The possible impacts of the parasitic secondary-phase LiV_2O_5 on the lithium ion intercalation performance have also been discussed.

Keywords Nitrogen annealing · Nickel-doped lithium trivanadate · Oxygen vacancies · Parasitic secondary phase

1 Introduction

Although lithium ion batteries are one of the most successful energy storage technologies and have enjoyed widespread applications in the past 2.5 decades, search for better electrode materials for energy storage technologies with increased energy and power density with improved cyclic stability at a reduced cost and with earth abundant materials has only got increasingly intensified [1–3]. Lithium trivanadate (LiV_3O_8, denoted as LVO) has been studied in the past years since the first research of its lithium ion intercalation capability by Wadsley [4]. It is considered as a viable cathode for moderate-voltage lithium ion batteries due primarily to its relatively large reversible lithium ion insertion/extraction capacity [5, 6]. However, its low electronic conductivity ($\sim 10^{-6}$ S cm^{-1}) and lithium ion diffusion coefficient ($\sim 10^{-10}$ cm^2 s^{-1}) have hindered its practical applications [7–9]. Materials with appropriately designed and fabricated nanostructures with a large specific surface area have demonstrated to offer more active reaction sites for lithium ions and obviously possess shortened diffusion length in the insertion/extraction process and thus presented much improved cycling performance and rate capability [10]. Similar to other layer-structured cathode materials, the capacity fade of LVO is often attributed to structural changes, phase transition and surface changes [11]. Surface coating and passivation of nanostructured electrodes have demonstrated to be an effective approach for improving cyclic stability of LVO during the insertion/extraction of lithium ions [12–14]. Doping in cathode materials has also demonstrated to effectively improve electrochemical properties. For example, Mo-doped LVO cathode has better reversibility than pure LVO [15]. Similarly, Ni doping in LVO resulted in much improved lithium ion intercalation properties because low-valence-state Ni can introduce oxygen vacancies that provide the nucleating sites and ion diffusion path in the phase transition of electrode materials during the charge/discharge process [16].

SPECIAL TOPIC: Materials for Energy Conversion

Y. Liu · C. Zhang · C. Liu · H. Song · X. Nan · G. Cao
Beijing Institute of Nanoenergy and Nanosystems, Chinese Academy of Sciences, Beijing 100083, China

G. Cao (✉)
Department of Materials and Engineering, University of Washington, Seattle, WA 98195-2120, USA
e-mail: gzcao@u.washington.edu

In addition to design and synthesis of nanostructures, carbon nanocoating and doping, the introduction of surface defects through controlled annealing in reducing gas is yet another approach to improve the lithium ion intercalation properties [17–20]. Liu et al. [19, 20] found that the presence of defects, such as V^{4+}, and associated oxygen vacancies could also improve the cycle life of LVO. The defects at the interface of LVO and electrolyte could possibly facilitate the phase transition during the insertion/extraction process due to modified surface thermodynamics [21, 22]. In addition, the presence of surface defects at LVO/electrolyte interface could preserve the integrity of cathode surface morphology, improving the cyclic stability of cathode materials [23]. Such surface defects in vanadium oxides can be readily introduced by annealing in an inert gas at elevated temperatures, such as in nitrogen gas at 300 °C [24, 25].

The present paper focuses on the effect of nitrogen annealing on the lithium ion intercalation properties of nickel-doped lithium trivanadate, a part of the efforts as to explore combined or even synergistic effects of doping and surface defects through annealing on the electrochemical properties, taking lithium trivanadate as a model system, as the impacts of nickel doping has been reported recently in a separate publication [16]. We first synthesized nickel-doped LVO (Ni-LVO) followed with annealing in air or nitrogen. The crystallinity, microstructures and lithium ion intercalation properties of the resulting Ni-LVO have been investigated, and the influence of the annealing atmosphere has been discussed. The experimental results revealed that Ni-LVO electrode annealed in nitrogen atmosphere exhibited improved electrochemical properties compared to that annealed in air, and the possible cause for such an improvement has been discussed.

2 Experimental

2.1 Material synthesis

All chemicals used in our work were analytical grade and were used without further purification. Previously reported procedure was modified to synthesize Ni-LVO [26]. V_2O_5, $CH_3COOLi·2H_2O$, $(CH_3COO)_2Ni·4H_2O$ and oxalic acid ($H_2C_2O_4·2H_2O$) were used as raw materials to prepare the precursor solution, oxalic acid acting as a both chelating and reducing agent. First, V_2O_5 and oxalic acid in a stoichiometric ratio of 1:3 were dissolved in deionized water under vigorous stirring at 400 r min^{-1} at room temperature until the color of solution turned from yellow to blue, which indicates that the valance state of V transformed from +5 to +4 and that vandyl oxalate hydrate

($VOC_2O_4·nH_2O$) formed [27]. The reaction can be expressed as shown [28]:

$$V_2O_5 + 3H_2C_2O_4 \rightarrow 2VOC_2O_4 + 3H_2O + 2CO_2$$

Then, a certain amount of $(CH_3COO)_2Ni·4H_2O$ in which nickel accounts for 5 % of vanadium was added into the solution. The color of solution turned dark green. A stoichiometric amount of $CH_3COOLi·2H_2O$ was added, and then the mixture was vigorously stirred (600 r min^{-1}) for 1 h. Finally, the mixture was dried overnight in an oven at 80 °C to get the powder. The as-obtained powders were then annealed at 300 °C in nitrogen for 2 h at a temperature ramping rate of 2 °C min^{-1} to get N-Ni-LVO. In contrast, we synthesized the powder and annealed at 300 °C in air in the same way to get A-Ni-LVO.

2.2 Material characterization

X-ray diffraction (XRD) analyses of the samples were conducted on a Marcogroup diffractometer (MXP21 VAHF) with a Cu-Kα radiation source ($\lambda = 1.54056$ Å). X-ray photoelectron spectroscopy (XPS) was performed on the Thermo Scientific ESCA Lab 250Xi using 200 W monochromated Al-Kα radiation. The 500-μm X-ray spot was used for XPS analysis. The base pressure in the analysis chamber was about 3×10^{-10} mbar (1 mbar = 100 Pa). Typically the hydrocarbon C 1s line at 284.8 eV from adventitious carbon was used for energy referencing. The morphologies of samples were investigated by HITACHI SU8200 cold field emission scanning electron microscope (FESEM). The total surface area was determined using nitrogen sorption analyses via surface area and porosity analyzer (Micromeritics ASAP 2020 HD88, USA). For the mesopore surface area, pore volume and pore diameter, the Barrett–Joyner–Halenda (BJH) method was adopted, whereas the specific surface area and the pore volume of micropores were calculated using t-method.

2.3 Electrochemical characterization

Electrochemical tests were carried out using 2032 coin cells assembled in an argon-filled glove box in which both the content of oxygen and water were below 0.5 ppm (parts per million). To prepare working electrodes, a mixture of active material, carbon black and poly-(vinyl difluoride) (PVDF) at a weight ratio of 80:10:10 was pasted on an Al foil. The electrolyte was composed of 1 mol L^{-1} LiPF$_6$ dissolved in a mixture of ethylene carbonate/dimethyl carbonate/diethyl carbonate (EC/DMC/DEC, 1:1:1 vol%, CAPCHEM). A Celgard polypropylene was used as the separator. To investigate the electrochemical properties of electrode materials, the half cells were adopted and lithium foil was used as the counter electrode.

SCIENCE CHINA PRESS

Galvanostatic charge–discharge tests of assembled cells were performed on a Land CT2001A system (Wuhan, China) under various current densities. The discharge/charge voltage window is 2.0–4.0 V versus Li$^+$/Li. Cyclic voltammograms (CVs) were conducted on a Solartron SI 1287 at the scanning rate of 0.1 mV s^{-1}. Electrochemical impedance spectroscopy (EIS) was conducted on a Solartron SI 1260 over the frequency range from 100 kHz to 0.1 Hz with an amplitude of 10 mV. Before the EIS test, the cells were charged to 2.8 V and then kept at that voltage for 10 min to reach a stable state. All electrochemical measurements were carried out at room temperature. The current densities for the half cells were all determined based on the mass of active materials on electrodes.

3 Results and discussion

3.1 Structural characterization

Figure 1a shows the XRD patterns of the samples N-Ni-LVO and A-Ni-LVO. The XRD peak positions of A-Ni-LVO are in agreement with the layered-type LiV$_3$O$_8$ (JCPDS 72-1193) [29]. However, sample N-Ni-LVO demonstrated appreciable difference in its XRD, though LiV$_3$O$_8$ remains the predominant phase. A parasitic secondary-phase LiV$_2$O$_5$ is evidently present (JCPDS 18-0756) [30] in the sample of N-Ni-LVO. Both XRD patterns revealed that the samples contain neither nickel metal nor NiO, for nickel is most likely to be incorporated to the LVO compound through substituting and taking vanadium ion positions, considering the relatively small amount of nickel doping (5 %) and reasonable difference in ionic radii of Ni^{2+} (70 pm with CN = 6, and higher valence nickel ions would have smaller radius) and V^{5+} (57 pm with CN = 6, and lower valence vanadium ion

would have larger radius). Doping of nickel in LVO has been elaborated in our earlier work [16], and Ni doping in vanadium pentoxide has also been reported [31]. There are obvious differences in the XRD patterns of A-Ni-LVO and N-Ni-LVO samples: the presence of LiV$_2$O$_5$ parasitic secondary phase and the shift of diffraction peaks to low angles in N-Ni-LVO sample. In LiV$_2$O$_5$, vanadium ions possess a valence state of 4.5+, instead of 5+ in LiV$_3$O$_8$. Although the exact mechanism leading to the formation of LiV$_2$O$_5$ is not known, the nitrogen annealing has obviously contributed to the valence reduction in vanadium ions. The appreciable shift of diffraction peaks in N-Ni-LVO, particularly at high angles, is an indication of expanded lattice constants, also suggesting the presence and/or increased amount of tetravalent vanadium ions.

XPS survey spectrum of N-Ni-LVO (Fig. 1b) shows the peaks of Li 1s, V 2p and O 1s clearly, but the peak of Ni 2p is not obvious due to its small quantity. Figure 1c is the high-resolution XPS of V 2p with fitting. The two main peaks at 524.7 and 517.5 eV could be ascribed to the spin orbitals splitting in the components, V^{5+} 2p$^{1/2}$ and V^{5+} 2P$^{3/2}$ [32], while the peaks associated with V^{4+} at 522.0 eV (V^{4+} 2p$^{1/2}$) and 516.6 eV (V^{4+} 2p$^{3/2}$) are clearly present [33]. The relative atomic ratio of V^{5+} and V^{4+} is approximately of 1.8:1, estimated based on the fitting peak areas. Although the exact amount of tetravalent vanadium ions requires more refined study, the existence of large concentration of V^{4+} corroborates the shifted peak positions in the XRD patterns and also explains the formation of parasitic secondary-phase LiV$_2$O$_5$. The presence of tetravalent vanadium ions is known to be beneficial to lithium ion intercalation [19] as it enhances the electronic conductivity, as electrons may hop between pentavalent and tetravalent vanadium ions, and increases the void space favoring the lithium ion diffusion, through generating oxygen vacancies to maintain the electroneutrality. Tetravalent vanadium ions and oxygen vacancies on the
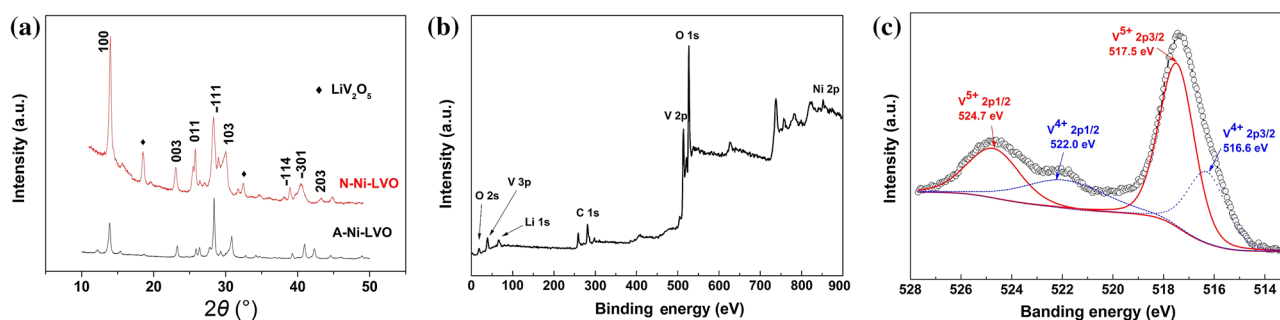
Fig. 1 (Color online) **a** XRD patterns of samples A-Ni-LVO and N-Ni-LVO, with the (100) peak positions aligned at the same angle for the sake of clear comparison. XPS spectra of N-Ni-LVO sample: **b** survey spectrum and **c** high-resolution V 2p spectrum, the measured curve was presented by the line with circles, and the fitting curves related to V^{4+} and V^{5+} were marked by dashed and solid lines, respectively

surface would affect the surface chemistry and the surface energy and thus may promote the intercalation and deintercalation reactions and the accompanied first-order phase transition.

Figure 2a, b shows the morphologies of A-Ni-LVO and N-Ni-LVO. The SEM image of A-Ni-LVO (Fig. 2a) shows that the nanosheets are 200–300 nm long, 100–200 nm wide and ~20 nm thick, with aggregation. In Fig. 2b, the particles have a smaller size where the sheets have 100–200 nm length, 50–100 nm width and ~20 nm thickness. Figure 2c, d shows the nitrogen sorption isotherms of samples A-Ni-LVO and N-Ni-LVO, from which the specific surface areas of two samples are calculated to be 30.0 and 35.4 $m^2 g^{-1}$, respectively. The pore volumes are also determined to be 0.188 and 0.208 $cm^3 g^{-1}$. The larger specific surface area and pore volume found in sample N-Ni-LVO are in good agreement with the SEM observation that N-Ni-LVO sample possessed smaller-sized particles. In general, larger specific surface area means more reaction sites, and smaller particle size means shorter diffusion distance, both of which are beneficial to lithium ion intercalation during the charge/discharge processes as well as the cyclic stability.

3.2 Electrochemical performance

Figure 3a compares the cyclic voltammograms or CV curves of A-Ni-LVO and N-Ni-LVO electrodes at a scan rate of 0.1 mV s^{-1} between 2.0 and 4.0 V versus Li^+/Li. During the cathodic scan of N-Ni-LVO electrode, there are five main peaks located at 2.34, 2.41, 2.51, 3.46 and 3.59 V, respectively. The peak at 3.59 V is related to the initial lithium ion inserted into the octahedral site of the LVO host structure [34]. The peaks at 2.41 and 2.51 V correspond to Li-ion insertion in the empty tetrahedral site with a single-phase reaction, and the peak around 2.34 V may relate to the two-phase transformation of $Li_3V_3O_8$/ $Li_4V_3O_8$ [35–39]. While the peak at 3.46 V may stem from the insertion reaction of LiV_2O_5 [30]. Also, there are five main peaks (2.48, 2.49, 2.66, 3.51 and 3.67 V) during the anodic scan of N-Ni-LVO. All the corresponding cathodic and anodic peaks are found in A-Ni-LVO sample; however, all the peaks in A-Ni-LVO are lower in peak intensity and broader in peak width than that in N-Ni-LVO samples. In addition, there is a clear relative shift of peak positions during both cathodic and anodic scans. In comparison with the peak positions in A-Ni-LVO sample, all the anodic
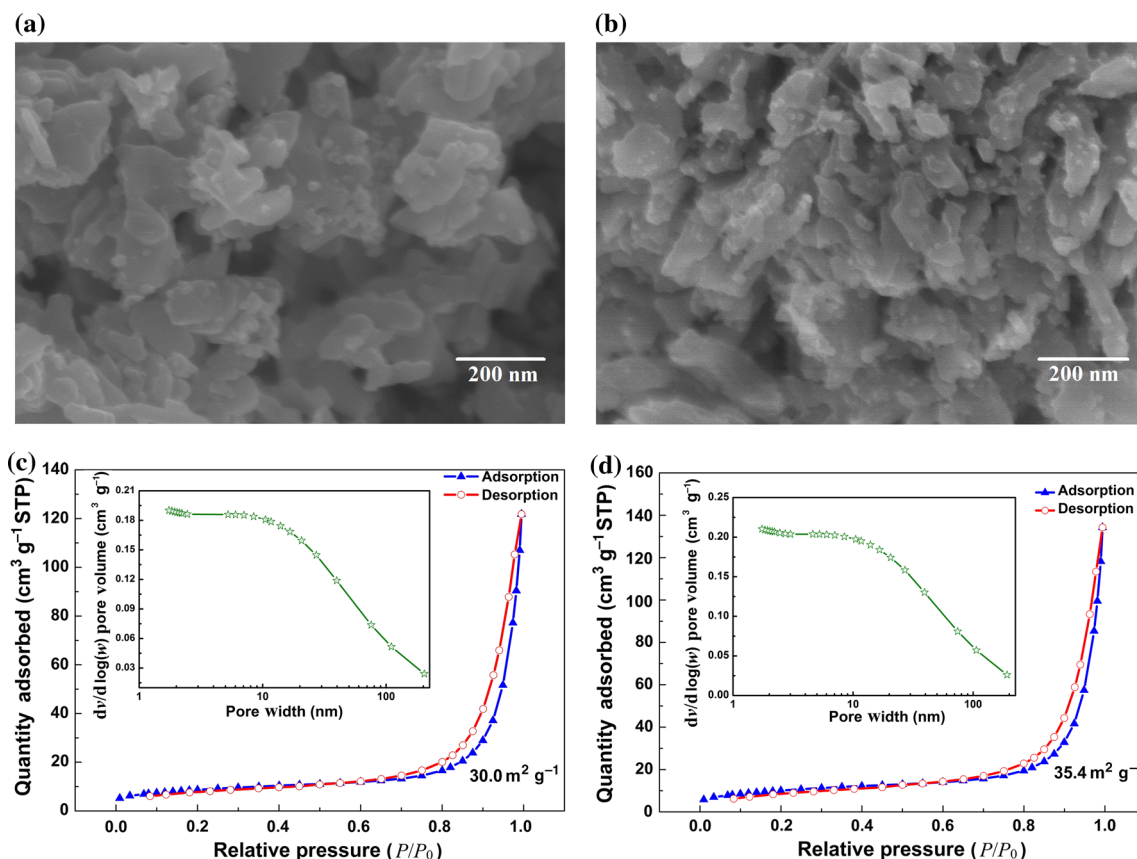
Fig. 2 (Color online) SEM images of **a** A-Ni-LVO and **b** N-Ni-LVO samples. The nitrogen sorption isotherms and corresponding BJH pore-size distribution curves (inset) of samples **c** A-Ni-LVO and **d** N-Ni-LVO
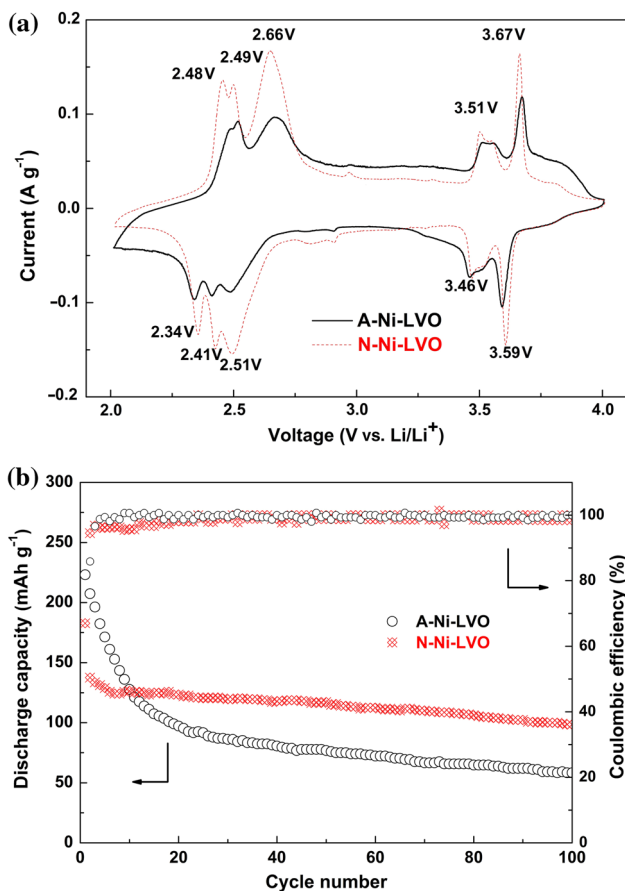
Fig. 3 (Color online) Electrochemical performance. **a** CV curves of the second cycle of A-Ni-LVO and N-Ni-LVO electrodes at a scan rate of 0.1 mV s^{-1} between 2.0 and 4.0 V versus Li$^+$/Li; **b** cycling performance of A-Ni-LVO and N-Ni-LVO electrodes at a current density of 1,500 mA g^{-1} (5 C) between 2.0 and 4.0 V

peaks in N-Ni-LVO have a left shift toward lower voltage and all the cathodic peaks have a right shift toward higher voltage. Consequently, the voltage intervals between the corresponding cathodic and anodic reactions reduce, a strong indication of much improved reversibility of lithium ion intercalation process in N-Ni-LVO sample as compared to A-Ni-LVO sample, possibly attributable to the change of surface energy and surface chemistry, i.e., the introduction or increased tetravalent vanadium ions and oxygen vacancies. Sharp peaks are indicative of better kinetics or transport properties, suggesting enhanced electronic conductivity and possible improved lithium ion diffusivity. The reduced voltage intervals between the corresponding redox peaks are also indicative of possible better kinetics, in addition to reduced energy barriers for intercalation and deintercalation reactions.

Figure 3b shows the cycling performance of A-Ni-LVO and N-Ni-LVO electrodes at a very high current density of 1,500 mA g^{-1} or 5 C between 2.0 and 4.0 V. A-Ni-LVO electrode delivered an initial discharge capacity of

223.1 mAh g^{-1}; however, it sharply decreases to 58.3 mAh g^{-1} after 100 cycles. By contrast, the N-Ni-LVO electrode shows much better cyclic stability. The initial discharge capacity of N-Ni-LVO is 182.8 mAh g^{-1} and remains 98.4 mAh g^{-1} after 100 cycles. It shows lower capacity fading than A-Ni-LVO electrode. Although the exact explanation for such a reduced capacity fading is not certain to us at this moment, there are several possible explanations. First, the existence of increased concentration of tetravalent vanadium ions, V^{4+}, would result in an enhanced electronic conductivity, and the corresponding oxygen vacancies would create more void space for lithium ion diffusion, so the voltage and composition polarization would be reduced. Second, the presence of tetravalent vanadium ions and oxygen vacancies at the surface would affect the surface dynamics and thus promote the insertion/extraction reaction and the accompanying phase transition. Third, the sample annealed in nitrogen atmosphere shows higher BET surface area with smaller particles, and it shortens the diffusion pathway for lithium ions so that the composition and the stress gradient are reduced. Lastly, the presence of parasitic secondary phase, LiV$_2$O$_5$, may serve as a buffer to circumvent the volume change associated with the lithium ion intercalation and deintercalation [39, 40]. Although the presence of the secondary phase in LVO cathode material is believed to improve its cyclic life, it is required to have more research to get a better fundamental understanding of the real mechanism.

Table 1 compares the rate performance of A-Ni-LVO and N-Ni-LVO electrodes. The current density increased from 0.2 to 5 C in a stepwise manner with 10 cycles at each current density. A-Ni-LVO electrode delivers capacities of 285, 225, 170 and 50 mAh g^{-1} at 0.2, 0.5, 1 and 5 C, respectively. In comparison, N-Ni-LVO electrode shows better rate performance with discharge capacity of 320, 240, 180 and 80 mAh g^{-1} at 0.2, 0.5, 1 and 5 C, respectively. The nitrogen annealing did improve the rate performance, though not so significantly. For example, at 5C, sample N-Ni-LVO retained a discharge capacity of 80 mAh g^{-1}, 25 % of the discharge capacity of 320 mAh g^{-1} at a rate of 0.2 C, that is noticeable higher than 17.5 % retention of the discharge capacity found in

Table 1 Comparison of rate performance of A-Ni-LVO and N-Ni-LVO samples: discharge capacity (mAh g^{-1}) of samples A-Ni-LVO and N-Ni-LVO at different rates ranging from 0.2 to 5 C with standard deviation

Rate	A-Ni-LVO (mAh g^{-1})	N-Ni-LVO (mAh g^{-1})
0.2 C	285 ± 15	320 ± 30
0.5 C	225 ± 5	240 ± 12
1 C	170 ± 9	180 ± 3
5 C	50 ± 4	80 ± 10

sample A-Ni-LVO, which decreased from 285 mAh g^{-1} at 0.2 C to 50 mAh g^{-1} at 5 C. In contrast, the cyclic stability and cycling stability of N-Ni-LVO are obviously improved by nitrogen annealing, and the contributions from vacancies play an essential role in these electrochemical enhancements as discussed above.

The EIS results of A-Ni-LVO and N-Ni-LVO electrodes in the form of Nyquist plots with a proposed equivalent circuit as an inset are presented in Fig. 4, which shows one depressed semicircle in the medium frequency range. The semicircle is attributed to the charge-transfer resistance (R_{ct}) [41, 42]. The ascending slope line represents the Warburg impedance (Z_w) at low frequency, indicating the diffusion rate of lithium ions in the solid matrix [41]. The fitted results of R_s and R_{ct} of A-Ni-LVO and N-Ni-LVO electrodes using the equivalent circuit in the inset are shown in Table 2. Obviously, the R_{ct} of the N-Ni-LVO electrode (72 Ω) is smaller than that of the A-Ni-LVO electrode (88 Ω). Such suppressed semicircle is considered as an important factor for the improvement of the active materials [43, 44]. Apparently, the sample annealed in nitrogen suppresses the charge-transfer resistance, thus resulting in improved electrochemical properties. The reduction in R_{ct} or the reduced charge-transfer resistance is a direct evidence of improved electronic conduction in sample N-Ni-LVO and enhanced surface chemistry, attributable to the presence of tetravalent vanadium ions and the accompanying oxygen vacancies, as well as large surface area and small crystal particle size.

4 Conclusions

Nitrogen annealing of Ni-doped lithium trivanadate N-LVO displayed high storage capacity, significantly improved cyclic stability, as N-Ni-LVO showed ∼70 % more remaining discharge capacity than A-Ni-LVO, and improved rate performance. Annealing in nitrogen resulted in the formation of parasitic secondary-phase LiV_2O_5 and created oxygen vacancies accompanied with V^{4+}, which resulted in an improved electronic conductivity and possibly enhanced lithium ion diffusivity. The combined effect of nitrogen annealing and Ni doping and the impacts of the presence of secondary-phase LiV_2O_5 require further study.

Conflict of interest The authors declare that they have no conflict of interest.

Fig. 4 (Color online) Nyquist plots of A-Ni-LVO and N-Ni-LVO electrodes at 2.8 V versus Li$^+$/Li

Table 2 Impedance parameters calculated from EIS results using the equivalent circuit from Fig. 4

Sample	R_s (Ω)	R_{ct} (Ω)
A-Ni-LVO	6	88
N-Ni-LVO	1.8	72

References

1. Yoo HD, Markevich E, Salitra G et al (2014) On the challenge of developing advanced technologies for electrochemical energy storage and conversion. Mater Today 17:110–121
2. Masse R, Uchaker E, Cao GZ (2015) Beyond Li-ion: electrode materials for sodium- and magnesium-ion batteries. Sci China Mater 58:715–766
3. Liu CF, Neale ZG, Cao GZ (2015) Understanding the electrochemical potential of electrodes in rechargeable batteries. Mater Today. doi:10.1016/j.mattod.2015.10.009
4. Wadsley AD (1957) Crystal chemistry of non-stoichiometric pentavalent vanadium oxides—crystal structure of $Li_{1+x}V_3O_8$. Acta Crystallogr 10:261–267
5. Pistoia G, Pasquali M, Wang G et al (1990) $Li/Li_{1+x}V_3O_8$ secondary batteries—synthesis and characterization of an amorphous form of the cathode. J Electrochem Soc 137:2365–2370
6. Zhang HL, Neilson JR, Morse DE (2010) Vapor-diffusion-controlled sol–gel synthesis of flaky lithium vanadium oxide and its electrochemical behavior. J Phys Chem C 114:19550–19555
7. Li Y, Fu ZY, Su BL (2012) Hierarchically structured porous materials for energy conversion and storage. Adv Funct Mater 22:4634–4667
8. Mai LQ, Xu X, Xu L et al (2011) Vanadium oxide nanowires for Li-ion batteries. J Mater Res 26:2175–2185
9. Whittingham MS (2008) Inorganic nanomaterials for batteries. Dalton Trans 40:5424–5431
10. Wang Y, Wang Y, Hosono E et al (2008) The design of a $LiFePO_4$/carbon nanocomposite with a core–shell structure and

its synthesis by an in situ polymerization restriction method. Angew Chem Int Ed 120:7571–7575

11. Jouanneau S, La Salle AL, Verbaere A et al (2005) The origin of capacity fading upon lithium cycling in $Li_{1.1}V_3O_8$. J Electrochem Soc 152:A1660–A1667

12. Qiu Q, Huang X, Chen YM et al (2014) Al_2O_3 coated $LiNi_{1/3}Co_{1/3}Mn_{1/3}O_2$ cathode material by sol–gel method: preparation and characterization. Ceram Int 40:10511–10516

13. Lee JH, Lee JK, Yoon WY (2013) Electrochemical analysis of the effect of Cr coating the LiV_3O_8 cathode in a lithium ion battery with a lithium powder anode. ACS Appl Mater Inter 5:7058–7064

14. Shin J, Jung H, Kim Y et al (2014) Carbon-coated V_2O_5 nanoparticles with enhanced electrochemical performance as a cathode material for lithium ion batteries. J Alloy Compd 589:322–329

15. Song HQ, Liu YG, Zhang CP et al (2015) Mo-doped LiV_3O_8 nanorod-assembled nanosheets as a high performance cathode material for lithium ion batteries. J Mater Chem A 3:3547–3558

16. Liu YG, Song HQ, Zhang CP et al (2015) Nickel-doped lithium trivanadate nanosheets synthesized by hydrothermal synthesis as high performance cathode materials for lithium ion batteries. Sci Adv Mater. doi:10.1166/sam.2015.2644

17. Zhang QF, Candelaria SL, Uchaker E et al (2013) Nanostructured materials for energy conversion and storage. Chem Soc Rev 42:3127–3171

18. Song L, Yang S, Wei W et al (2015) Hierarchical SnO_2 nanoflowers assembled by atomic thickness nanosheets as anode material for lithium ion battery. Sci Bull 60:892–895

19. Liu D, Liu Y, Garcia BB (2009) V_2O_5 xerogel electrodes with much enhanced lithium-ion intercalation properties with N_2 annealing. J Mater Chem 19:8789–8795

20. Liu DW, Liu YY, Pan AQ et al (2011) Enhanced lithium-ion intercalation properties of V_2O_5 xerogel electrodes with surface defects. J Phys Chem C 115:4959–4965

21. Swider-Lyons KE, Love CT, Rolison DR (2002) Improved lithium capacity of defective V_2O_5 materials. Solid State Ionics 152:99–104

22. Ganduglia-Pirovano MV, Sauer J (2004) Stability of reduced V_2O_5 (001) surfaces. Phys Rev B 70:045422

23. Subramanian V, Zhu HW, Wei BQ (2006) High rate reversibility anode materials of lithium batteries from vapor-grown carbon nanofibers. J Phys Chem B 110:7178–7183

24. Wu QH, Thissen A, Jaegermann W et al (2004) Photoelectron spectroscopy study of oxygen vacancy on vanadium oxides surface. Appl Surf Sci 236:473–478

25. Li ZY, Wu QH (2008) The effects of oxygen vacancies on the electronic properties of V_2O_{5-x}. J Mater Sci Mater Electron 19:S366–S370

26. Pan AQ, Zhang JG, Cao GZ et al (2011) Nanosheet-structured LiV_3O_8 with high capacity and excellent stability for high energy lithium batteries. J Mater Chem 21:10077–10084

27. Pan AQ, Wu HB, Yu L et al (2012) Synthesis of hierarchical three-dimensional vanadium oxide microstructures as high-capacity cathode materials for lithium-ion batteries. ACS Appl Mater Interface 4:3874–3879

28. Pan AQ, Liu J, Zhang JG et al (2011) Template free synthesis of LiV_3O_8 nanorods as a cathode material for high-rate secondary lithium batteries. J Mater Chem 21:1153–1161

29. Liu YM, Zhou XC, Guo YL (2008) Effects of reactant dispersion on the structure and electrochemical performance of $Li_{1.2}V_3O_8$. J Power Sources 184:303–307

30. Wang WJ, Wang HY, Liu SQ et al (2012) Synthesis of gamma-LiV_2O_5 nanorods as a high-performance cathode for Li ion battery. J Solid State Electronchem 16:2555–2561

31. Zheng YZ, Ding HY, Uchaker E (2015) Nickel-mediated polyol synthesis of hierarchical V_2O_5 hollow microspheres with enhanced lithium storage properties. J Mater Chem A 3:1979–1985

32. Sawatzky GA, Post D (1979) X-ray photoelectron and auger-spectroscopy study of some vanadium-oxides. Phys Rev B 20:1546–1555

33. Feng Y, Li YL, Hou F (2009) Boron doped lithium trivanadate as a cathode material for an enhanced rechargeable lithium ion batteries. J Power Sources 187:224–228

34. Sarkar S, Banda H, Mitra S (2013) High capacity lithium-ion battery cathode using LiV_3O_8 nanorods. Electrochim Acta 99:242–252

35. Xu X, Luo YZ, Mai LQ et al (2012) Topotactically synthesized ultralong LiV_3O_8 nanowire cathode materials for high-rate and long-life rechargeable lithium batteries. Npg Asia Mater 4:e20

36. Kawakita J, Katayama Y, Miura T et al (1998) Structural properties of $Li_{1+x}V_3O_8$ upon lithium insertion at ambient and high temperature. Solid State Ionics 107:145–152

37. Kawakita J, Miura T, Kishi T (1999) Charging characteristics of $Li_{1+x}V_3O_8$. Solid State Ionics 118:141–147

38. Kawakita J, Miura T, Kishi T (1999) Lithium insertion and extraction kinetics of $Li_{1+x}V_3O_8$. J Power Sources 83:79–83

39. Sun D, Xu G, Wang H et al (2015) Multi-layered $Al_2O_3/Li_xV_2O_5/LiV_3O_8$ nanoflakes with superior cycling stability as cathode material for Li-ion battery. Electrochim Acta 157:211–217

40. Sun D, Jin G, Wang H et al (2014) $Li_xV_2O_5/LiV_3O_8$ nanoflakes with significantly improved electrochemical performance for Li-ion batteries. J Mater Chem A 2:8009–8016

41. Wang HY, Huang KL, Ren Y et al (2011) $NH_4V_3O_8$/carbon nanotubes composite cathode material with high capacity and good rate capability. J Power Sources 196:9786–9791

42. Kang YJ, Kim JH, Lee SW et al (2005) The effect of $Al(OH)_3$ coating on the $Li[Li_{0.2}Ni_{0.2}Mn_{0.6}]O_2$ cathode material for lithium secondary battery. Electrochim Acta 50:4784–4791

43. Idris NH, Rahman MM, Wang JZ et al (2011) Synthesis and electrochemical performance of LiV_3O_8/carbon nanosheet composite as cathode material for lithium-ion batteries. Compos Sci Technol 71:343–349

44. Sun YK, Han JM, Myung ST et al (2006) Significant improvement of high voltage cycling behavior AlF_3-coated $LiCoO_2$ cathode. Electrochem Commun 8:821–826